
Article:
Ma, X.Y., Li, G. orcid.org/0000-0002-5956-4033, Jewell, G.W. et al. (2 more authors) (2016) Performance comparison of doubly salient reluctance machine topologies supplied by sinewave currents. IEEE Transactions on Industrial Electronics, 63 (7). 7437424. pp. 4086-4096. ISSN 0278-0046

https://doi.org/10.1109/TIE.2016.2544722

Performance Comparison of Doubly Salient Reluctance Machine Topologies Supplied by Sinewave Currents

X. Y. Ma, G. J. Li, Member, IEEE, G. W. Jewell, Z. Q. Zhu, Fellow, IEEE, and H. L. Zhan

Abstract—This paper comprehensively investigates the electromagnetic performance of 3-phase, 12-slot, and 8-pole switched reluctance machines (SRMs) with different winding configurations, i.e. double/single layer, short pitched (concentrated) and fully pitched (distributed). These SRMs are supplied by sinewave currents so that a conventional 3-phase converter can be employed, leading to behavior which is akin to that of synchronous reluctance type machines. Comparisons in terms of static and dynamic performances such as d- and q-axis inductances, on-load torque, torque-speed curve, efficiency map, etc. have been carried out using two-dimensional finite element method (2-D FEM). It is demonstrated for the given size of machine considered, that for same copper loss and without heavy magnetic saturation, both single and double layer mutually coupled SRMs can produce higher on-load torque compared to conventional SRMs. Additionally, double layer mutually coupled SRM achieved the highest efficiency compared to other counterparts. When it comes to single layer SRMs, they are more suitable for middle speed applications and capable of producing higher average torque while lower torque ripple than their double layer counterparts at low phase current. Two prototype SRMs, both single layer and double layer, are built to validate the predictions.

Keywords—Double/single layer, fully/short-pitched, mutually coupled, switched/synchronous reluctance machine.

I. INTRODUCTION

Nowadays, SRMs are predominately used in a variety of applications in the automotive, renewable energy, aerospace and domestic appliances sectors. [1] [2]. This is mainly due to the fact that there are neither permanent magnets nor field windings on the rotor. As a result, the SRMs can be low cost and have simple and robust rotor structure compared to other electrical machines, and hence suitable for harsh environment and safety-critical applications [1] [3] [4]. Despite these and other attractive features, SRMs have arguably yet to gain the foothold in the market that one might have expected. One important limiting factor for conventional SRMs is that the power converter stage is nonconventional.

In addition, SRMs tend to exhibit high levels of acoustic noise and vibration due to doubly salient structure and unipolar phase current waveforms. This has to some extent, limited their wider industrial application [5]. It is well-established that the main source of vibration and consequent acoustic noise is the abrupt change of radial magnetic force around the air gap. In addition, the stator vibration can also be excited by torque ripple, subsequently emitting acoustic noise [6]. This is particularly the case for low speed conditions. In order to reduce the vibration and acoustic noise, several noise mitigation strategies have been proposed in literature such as stator lamination shape optimization [7], rotor and stator skewing [8], hybrid excitation with a C-dump inverter to reduce the rapid change of radial magnetomotive force (mmf) [9], two-stage commutation [10], voltage smoothing using pulse-width modulation (PWM) [11], and active vibration damping using piezoelectric actuators [12] [13].

Furthermore, lower vibration and noise levels can also be achieved by using the mutually coupled SRMs [14], especially supplied by sinewave currents as demonstrated in [5], [15] and [16]. Moreover, the well-established three-phase inverter topology, of the type used for synchronous and induction machines can be used as shown in Fig. 1. Moreover, the classical PI controller can be used for current control. This paper is focused on SRMs supplied with sinewave currents. It is worth noting that the SRMs supplied by sinewave currents are in effect short-pitched synchronous reluctance machines (SynRMs) while classic SynRMs often employ distributed windings to achieve higher saliency and hence higher reluctance torque. However, to be consistent with terminology which is widely used in the literature, they will be referred to throughout this paper as SRMs.

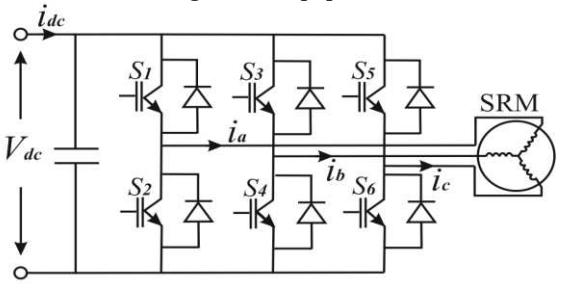

Fig. 1. Standard 3-phase inverter for sinewave excitation [16].

It is well-established that, the double layer mutually coupled SRM (MCSRM) are less sensitive to magnetic saturation and consequently, on a like-for-like basis, produce higher average torque than double layer conventional SRM (CSRM) at high phase current [17] with enhancement of the order around 77% up to $40A_{rms}$ [18]. However, the torque ripple of MCSRM is relatively higher because of the nature of self- and mutual inductance variations, and hence can potentially generate higher noise at low speed.

This issue can be mitigated by using the single layer fully-pitched SRM (FPSRM) [18] [19]. However, its considerably longer end-windings result in an increased overall machine envelope and higher copper loss for a given phase current. To combine the merits of both the single layer FPSRM (high torque capability) and the double layer MCSRM (short end-winding), two short-pitched, single layer winding SRMs have been proposed and compared with the double layer SRMs and FPSRM in [18].

Manuscript received August 26, 2015; revised September 4, 2015, November 23, 2015, and February 14, 2016; accepted February 19, 2016.
X. Y. Ma, G. J. Li, G. W. Jewell, Z. Q. Zhu and H. L. Zhan are with the Electrical machines & Drives (EMD) Group, University of Sheffield, Sheffield, UK (g.li@sheffield.ac.uk)

II. Machine Topologies and Winding Configurations

A. Established configurations of SRMs

As previously mentioned, different winding configurations have significant influences on the electromagnetic performances of SRMs. To investigate this behavior, 3-phase, 12-slot/8-pole SRMs with two different short-pitched windings (CSRM and MCSRM) and one fully-pitched winding (FPSRM) have been considered. The leading machine dimensions and key design features are summarized in TABLE I. Cross-sections through these three machine designs are shown in Fig. 2, in which "-" represents a GO conductor while "+" represent a RETURN conductor. The machine dimensions have been optimized for the conventional single layer SRM supplied by sinewave current. To simplify the comparison, all SRMs have adopted the same dimensions. It is worth mentioning that the individual optimization of some SRM will slightly improve their output torque by less than 10% compared to the dimensions adopted in this paper.

TABLE I MACHINE LEADING DIMENSIONS AND DESIGN FEATURES

Stator slot number	12	Active length (mm)	60
Rotor pole number	8	Turn number per phase	132
Stator outer radius (mm)	45	Coil packing factor	0.37
Air gap length (mm)	0.5	Rated RMS current (A)	10
Rotor outer radius (mm)	26.5	Current density (A_{rms}/mm^2)	5.68
Rotor inner radius (mm)	15.7		

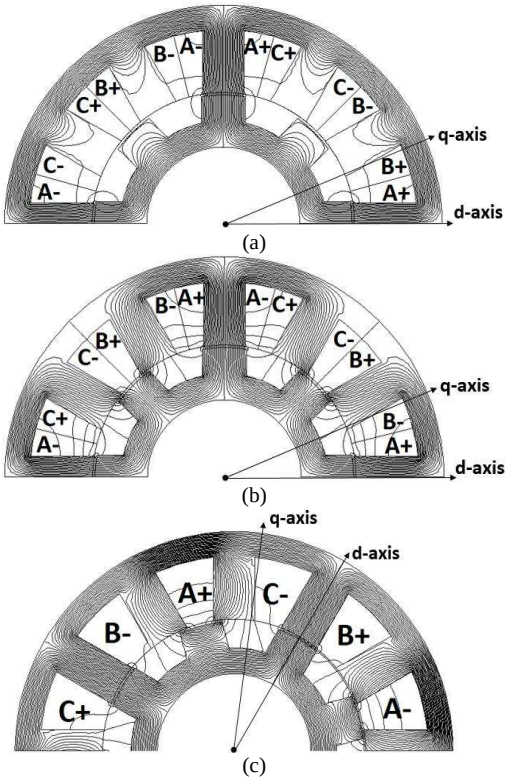

Fig. 2. Comparison of flux line distributions when phase A is supplied by a 10A dc current. (a) CSRM. (b) MCSRM. (c) FPSRM.

For both the CSRM and MCSRM, each phase winding consists of 4 concentrated coils, and each stator tooth is wound with one coil. As a result, two coils belonging to two different phases are located in a given stator slot, leading to, at least in terms of mmf distribution, an arrangement akin to a double layer winding. This also dictates that the coil pitch is equal to the slot pitch ($2\pi/N_s$ where N_s is the stator slot number), which is smaller than the pole pitch ($2\pi/N_r$ where N_r is the rotor number). Hence, this gives rise to a short-pitched winding. In addition, the magnetic polarities of the coils of one phase, e.g. phase A, for the CSRM are SNSN, while for MCSRM, they are SSSS.

In contrast, for the FPSRM, each phase winding comprises 2 coils and each coil spans 3 slot pitches, leading to a fully-pitched winding. Moreover, it can be regarded as a single layer winding since only one coil is located in a given stator slot and the coil magnetic polarities of phase A are NS. However, as a consequence of the fully pitched winding, the end-windings of FPSRM will be significantly longer than those of a corresponding short pitched SRMs, in turn leading to higher copper loss.

The comparison in terms of flux distribution for the three SRMs configurations is shown in Fig. 2, in which only the phase A is supplied by a 10A dc current with the rotors in the aligned position. It will be apparent that there is little mutual coupling flux between phases in the CSRM, as shown in Fig. 2 (a). However, as will be apparent from Fig. 2 (b) and (c), the fluxes of phase A in MCSRM and FPSRM also link the coils of phase B and phase C. As a consequence, appreciable mutual flux is present and this will contribute to torque generation as noted previously and has been detailed in [17] and [20].

B. Proposed Single Layer SRM configurations

The winding configurations of the two single layer SRMs were designed based on the aforementioned double layer, short-pitched CSRM and MCSRM, as shown in Fig. 3.

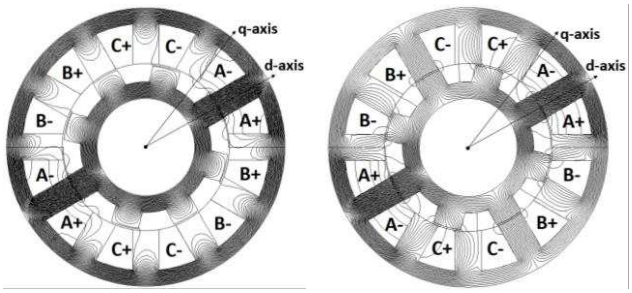

Fig. 3. Comparison of winding configuration and magnetic flux distributions between (a) SLCSRM and (b) SLMCSRM. The rotor is at aligned position and phase A is supplied by a 10A dc current.

Similarly, the coil magnetic polarities of phase A are NS for single layer CSRM (SLCSRM, similar to the double layer CSRM) and NN for single layer MCSRM (SLMCSRM, similar to the double layer MCSRM). Each phase of the single layer SRMs comprises 2 coils and each coil is wound around one stator tooth, leading to concentrated winding structure. As a result, their end-windings are significantly shorter than a correspondingly sized FPSRM. Moreover, similar to the FPSRM, the single layer SRMs also have one coil located in one stator slot, and can potentially have higher inductance variation against rotor position (number of turns per phase is the same for all SRMs) and hence higher torque production, as will be investigated later.

The magnetic flux distribution in the aligned position between SLCSRM and SLMCSRM is shown in Fig. 3, for the case in which phase A is supplied by a 10A dc current. As was the case with the double layer, short-pitched SRMs discussed above, appreciable mutual flux is only present in the SLMCSRM. However, for the same stator and rotor core dimensions, these two SRMs exhibit a higher degree of

magnetic saturation at the rated 10A dc current in phase than the case with their double layer counterparts. This can be attributed to the fact that although the single layer SRMs have half the number of coils compared to their double layer counterparts, the number of turns per coil is necessarily doubled to maintain the same number of turns per phase. This leads to higher spatial concertation of mmf. Thus, SLCSRM and SLMCSRM, in particular the former, are more sensitive to magnetic saturation and hence will have lower short-term overload torque capability.

It is worth mentioning that in this paper, for all the static performance investigations such as average torque vs current or copper losses, iron losses, etc. the ABC frame has been used [21], [5]. However, in order to simplify the investigation of dynamic performances such as torque speed characteristics and efficiency map, the dq frame has been employed [22].

III. Static Performance Investigation for SRMs

A. d- and q- Axis Inductances

As is the case for conventional SynRMs, the average electromagnetic torque of SRMs can be determined not only from the change in co-energy but also by the d- and q-axis inductances. Therefore, the well-established phasor diagram of SynRMs shown in Fig. 4 can be employed to analyze the SRMs supplied with sinewave currents. This diagram illustrates the relationship between d- and q-axis currents and the stator phase current I_{ph}, as well as the relationship between d- and q-axis voltages and the phase voltage V_{ph} [23]- [24]. In the phasor diagram, α corresponds to the phase advanced angle of I_{ph} with respect to the d-axis and, $\emptyset$ corresponds to the phase angle between I_{ph} and V_{ph}.

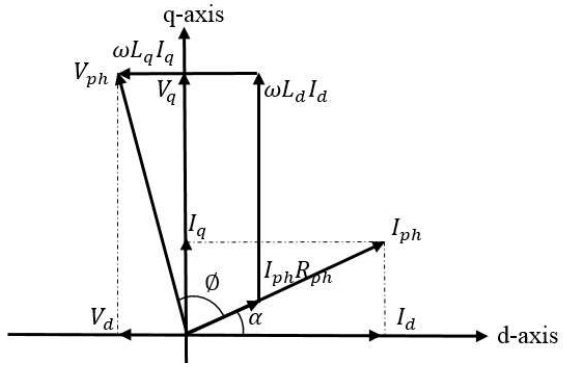

Fig. 4. Phasor diagram of synchronous reluctance motor [24].

According to the phasor diagram, the d- and q-axis inductances L_d and L_q, with due account of the influence of cross-coupling, are given by:

$$L_d(i_d, i_q) = \frac{\psi_d(i_d, i_q)}{i_d} \quad (1)$$

$$L_q(i_d, i_q) = \frac{\psi_q(i_d, i_q)}{i_q} \quad (2)$$

The d- and q-axis voltage V_d and V_q can be obtained as

$$V_d = R_{ph} I_d - \omega \psi_q \quad (3)$$

$$V_q = R_{ph} I_q + \omega \psi_d \quad (4)$$

where ψ_d and ψ_q are the d- and q-axis stator flux linkages, respectively. i_d and i_q are the d- and q-axis stator currents, respectively. R_{ph} is the phase resistance and ω is the electrical angular velocity of the supply.

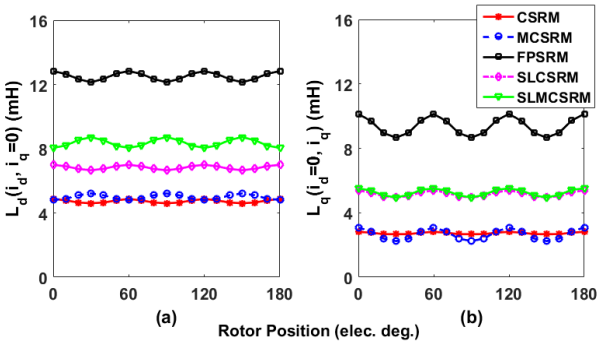

Fig. 5. Variation in (a) d-axis inductance $L_d(I_d, I_q = 0)$, and (b) q-axis inductance $L_q(I_d = 0, I_q)$ as a function of rotor position for a phase RMS current of 10A.

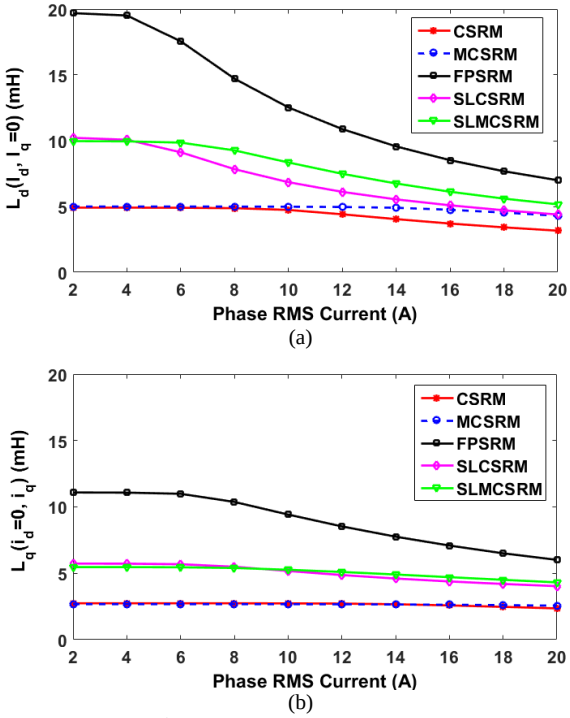

Fig. 6. Comparison of d- and q-axis inductances between SRMs. (a) d-axis inductance $L_d(I_d, I_q = 0)$, (b) q-axis inductance $L_q(I_d = 0, I_q)$.

The variation in $L_d(I_d, I_q = 0)$ and $L_q(I_d = 0, I_q)$ with rotor position and phase RMS current for all SRMs have been calculated by 2-D FEM. The resulting characteristics are shown in Fig. 5 and Fig. 6 respectively, from which it will be apparent that the highest d- and q-axis inductances are present in the FPSRM. Moreover, the d- and q-axis inductances of single layer CSRM and MCSRM are higher than that of their double layer counterparts. In terms of overload capability, Fig. 6 demonstrates that in all single layer SRMs, the onset of discernable magnetic saturation occurs at lower currents than the corresponding double layer SRM configurations (as indicated by the current at which the inductances begin to decline). This is again due to higher concentrated armature mmf, and hence a greater sensitivity to magnetic saturation than the corresponding double layer machines.

It is worth noting that the difference between L_d and L_q can be used to determine the electromagnetic torque capability. In order to predict the torque, (L_d-L_q) has been calculated at $\alpha = 45°$, with $I_d = I_q$, as shown in Fig. 7. As

will be apparent, the difference between d- and q-axis inductances is greatest in the case of the FPSRM. Hence, for the particular size of stator and rotor core, the FPSRM will produce the highest torque in the absence of significant magnetic saturation. Similarly, the single layer SRMs will produce higher torque than double layer SRMs without saturation due to the higher d-q axis inductances difference.

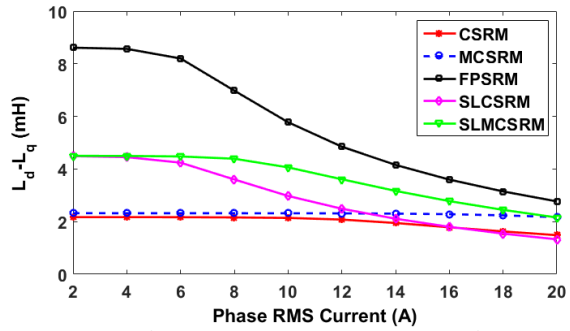

Fig. 7. Comparison of (L_d-L_q) between the SRMs at $\alpha = 45°$.

B. Average Torque vs Current Phase Advanced Angle

Having established d- and q-axis inductances, the torque produced by a 3-phase synchronous reluctance machine can be calculated from [25]:

$$T = \frac{3}{2} \times p(L_d - L_q) I_d I_q \tag{5}$$

This expression can also be applied to the many variants of SRMs considered in this paper when supplied by sinewave currents. Also, the d- and q-axis currents can be expressed in terms of the stator peak current yielding:

$$T = \frac{3}{4} \times p(L_d - L_q) {I_s}^2 sin2\alpha \tag{6}$$

where p is pole-pair number, I_s is stator peak current, and α is current phase advanced angle which influences the relationship between phase current i and rotor position θ, for instant of phase A $i_a = I_{rms} \sin(\theta - \alpha)$. It will be apparent from this expression that without magnetic saturation, the maximum average torque is achieved when $\alpha = 45°$. However, with the onset of d-axis saturation, the maximum average torque will be obtained at values of α greater than 45° [24].

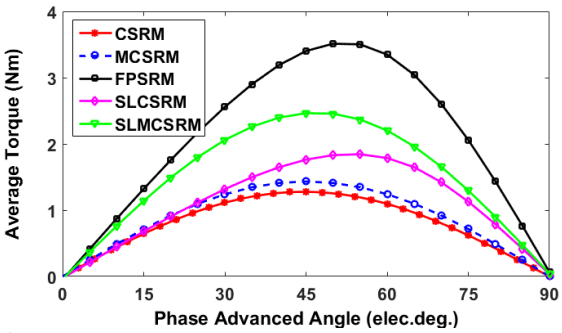

Fig. 8. Variation in average torque as a function of current phase advanced angle α for a phase RMS current of 10A.

A comparison of average torque as a function of α between the different SRMs configurations is shown in Fig. 8, a sinewave current of $10A_{rms}$ is applied in each case. As would be expected, under this excitation condition, the FPSRM produces the highest average torque. For the remaining topologies, the SLCSRM and SLMCSRM produce higher torque than their double layer counterparts. Additionally, the maximum average torques are generated at $\alpha = 45°$ for CSRM, MCSRM and SLMCSRM at $10A_{rms}$. However, for FPSRM and SLCSRM, the maximum average torques are achieved at 50° and 55°, respectively, behavior which is indicative of magnetic saturation even at this modest excitation levels.

C. Average Torque and Torque Ripple as a Function of Phase RMS Current

The comparisons in terms of average torque and torque ripple coefficient against phase RMS current have been carried out, as shown in Fig. 9, in which the torque ripple coefficient is calculated by

$$T_{ripple} = \frac{T_{max} - T_{min}}{T_{av}} \times 100\% \tag{7}$$

where T_{max}, T_{min} and T_{av} are the maximum, minimum and average torque for an electrical period, respectively.

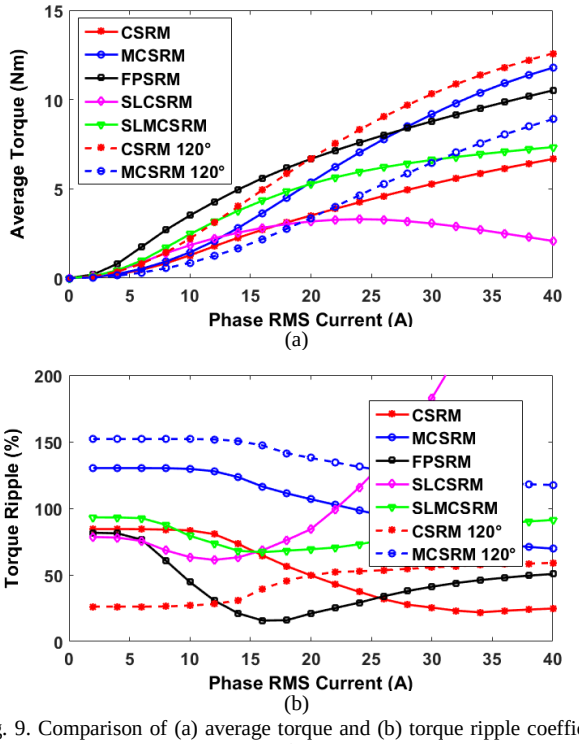

Fig. 9. Comparison of (a) average torque and (b) torque ripple coefficient against phase RMS current varying from 0A to 40A. (Solid lines stand for machines supplied by 3-phase sine wave currents. Performances of CSRM and MCSRM also compare to that supplied by conventional 120 elec. deg. square wave current.)

It is found that at low current, FPSRM produces higher average torque but lower torque ripple than the other SRMs. Additionally, the SLMCSRM and SLCSRM generate higher average torque but lower torque ripple than their double layer counterparts, as expected. However, at high current, average torque of double layer MCSRM exceeds that of FPSRM, because the FPSRM is more sensitive to magnetic saturation due to single layer winding structure. Similarly, at even higher phase current, both the SLCSRM and SLMCSRM produce less torque but potentially higher torque ripple than their relevant double layer counterparts. Therefore, it can be concluded that all FPSRM, SLCSRM and SLMCSRM present superior performances at low current. However, the FPSRM has significant longer end-winding than both

SLCSRM and SLMCSRM, leading to much higher copper loss.

For completeness, the results for SRMs supplied by conventional square wave current with unipolar 120 elec. deg. conduction are compared with that obtained using sinewave currents, as shown in Fig. 9. Here, the CSRM and MCSRM have been selected as examples. It is found that the CSRM supplied by square wave current can exhibit better performance, particularly at high phase current. However, it requires special converters, which is one of the main drawbacks of this machine type.

D. Copper Loss

With different winding structures, the copper losses of short/fully pitched, double/single layer SRMs will be different at the same phase current due to different end-winding structures. The average value of one end-winding length of short-pitched SRMs is assumed to be $\frac{1}{2}k\pi W_s + W_t$, where W_s is average stator slot width (trapezoidal) and W_t is stator tooth width. Coefficient k depends on the double layer (k=0.5) or single layer (k=1) winding configurations. For FPSRM, the end winding consists of $\frac{1}{2}k\pi W_s$ plus an arc length of the span range of a coil and it is given by:

$$End\ Winding = \frac{1}{2}k\pi W_s + 2\pi(S_i + \frac{1}{2}h_s) \times \frac{360°/N_s \times 3 - \gamma}{360°} \quad (8)$$

where k=1 due to its single layer structure, S_i is stator inner radius, h_s is slot height, N_s is number of slots, and γ is slot opening in mechanical degree

TABLE II COMPARISON OF COPPER LOSS WITH COIL TEMPERATURE OF 60℃ AT 10 A_{RMS}

Items	Double layer	Single layer	
	CSRM& MCSRM	FPSRM	SLCSRM& SLMCSRM
Mean length per turn (m)	0.15	0.32	0.18
Copper wire Length (m)	19.51	42.79	23.18
Phase resistance (Ω)	0.59	1.29	0.70
Rated copper loss (W)	177	387	210
Average torque (Nm)	1.28&1.45	3.51	1.84&2.46
Average torque per unit copper loss (Nm/W)	0.00723& 0.00819	0.00907	0.00876& 0.0117

TABLE II shows a comparison of copper loss between the SRMs under rated condition for a coil temperature of 60°C (assume test temperature to be 60°C). The nature of the end-windings in a FPSRM dictate that for this relatively short axial length of stator core, the total mean length per turn is more than doubled compared to the corresponding double layer winding SRMs, with consequent adverse implications for the phase resistance of the FPSRM. However, since the SLCSRM and SLMCSRM have similar short-pitched winding structures to their double layer counterparts, the penalty of resistance in these machines is much smaller.

However, as shown in TABLE II, the torque per unit copper loss of the FPSRM is still competitive with the other SRMs topologies. Indeed, in terms of torque per unit copper loss, there is a relatively narrow spread of values across the various machines. It is important to recognize that the aspect ratio of the stator core, i.e. length to diameter ratio, needs to be borne in mind when considering the relative merits of these topologies, since end-windings play a major role. Nevertheless, the SLCSRM and SLMCSRM, especially the latter, can achieve comparable torque against copper loss performance to the FPSRM but with much shorter end-winding and also smaller volume, especially at low average torque level as shown in [18]. However, to achieve a high average torque, the copper loss of the FPSRM is much higher than that of the MCSRM. It is also worth noting that both the CSRM and SLCSRM have the worst torque against copper loss performance [18].

E. Iron Loss

The different winding arrangements will also influence the nature of the flux distribution within the SRMs hence the magnitude of iron losses within stator and rotor iron cores. The calculation of iron losses in variable reluctance machines is very challenging, particularly in conventional switched reluctance machines operated with unipolar currents. In such machines, different regions of the stator and/or rotor core can be exposed to localized flux density waveform that can be unipolar, asymmetric AC waveforms and contain significant minor-loop excursions [26] [27].

For the machine topologies considered in this paper, the use of sinusoidal current simplifies the process for estimating iron loss, although many localized flux density are still likely to depart from sinusoidal.

In order to predict the iron loss, there are many methods presented in [28]. In this paper, the average iron loss density over one electrical cycle in a given region of the machine is estimated using equation (9) which is based on a simplified consideration of hysteresis and eddy current component of loss [21].

$$p_{iron}\ (W/m^3) = f\left(k_{h1}\Delta B_{pp} + k_{h2}\Delta {B_{pp}}^2\right) + k_e f \int_0^{1/f} (\frac{\partial B}{\partial t})^2 dt \quad (9)$$

where

f	Stator or rotor flux density frequency;
B_{pp}	Peak to peak value of flux density;
$k_{h1}\ and\ k_{h2}$	Hysteresis loss coefficients;
k_e	Eddy current loss coefficient.

For the Silicon iron cores considered in this series of the machines, the material specific coefficients take the values: $k_{h1} = 5A/m$, $k_{h2} = 40A/m$, and $k_e = 0.022\ Am/V$.

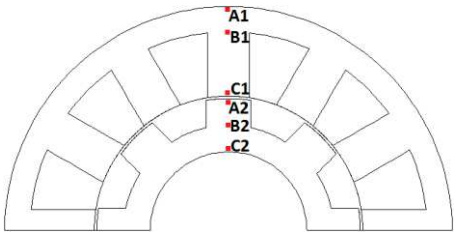

Fig. 10. Cross-section of 12-slot/8-pole SRM. Point A1, B1, and C1 are used for stator flux density observation. Point A2, B2, and C2 are used for rotor flux density observation.

The total iron loss is obtained from a summation of the iron losses calculated in every individual FE mesh element of the stator and rotor. When applying equation (9), it is necessary to recognize that at a given rotor speed, the flux density variations in the stator and rotor are at different frequencies.

By way of illustration, a series of flux density loci at the series of six locations defined in Fig. 8 have been selected to

determine the stator and rotor flux density frequencies. The resulting frequencies for the various machine topologies are summarized in TABLE III. For all the topologies considered, the stator flux density frequencies f_0 are the same and it is given by $\frac{\Omega p}{60}$, where Ω is mechanical rotor speed, and p is pole-pair number.

In contrast, the rotor flux density frequencies are different in the various topologies as summarized in Table III. For the double layer CSRM and MCSRM, the effective rotor frequency is twice than that of their single layer counterparts. In addition, the rotor flux density frequencies of both single and double layer MCSRMs are twice than that of CSRMs.

TABLE III FLUX DENSITY FREQUENCY

Machine types	Stator B_r/B_t frequency (Hz)	Rotor B_r/B_t frequency (Hz)
FPSRM	f_0	$1.5f_0$
CSRM	f_0	$1.5f_0$
MCSRM	f_0	$3f_0$
SLCSRM	f_0	$0.75f_0$
SLMCSRM	f_0	$1.5f_0$

The different rotor flux density frequencies dictate that the relative merits of the different machines in terms of their rotor iron losses cannot simply be gauged from the selected rotor flux density loci (hence not present in this paper). Recourse to a full calculation of iron loss throughout the stator and rotor by the application of equation (9) over on repeating cycle in every element of the FE mode is required. To this end, the iron losses for the reference designs of all machine types being considered were calculated for sinewave current of $10A_{rms}$ at $400\ rpm$.

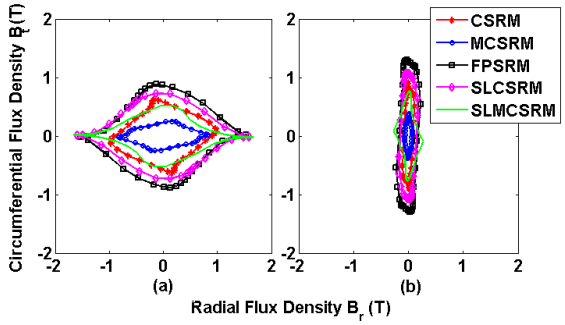

Fig. 11. Comparison of radial and circumferential stator flux densities of the SRMs, at 400rpm, supplied by 10A phase RMS current. (a) Point A1. (b) Point B1 in Fig. 10. B_t is the circumferential component while B_r is the radial component of flux density.

TABLE IV IRON LOSS AT RATED CURRENT, 400 RPM

Machine types	Stator iron loss (W)	Rotor iron loss (W)	Total iron losses (W)
CSRM	1.07	1.15	2.22
MCSRM	0.57	0.24	0.81
FPSRM	2.24	2.45	4.69
SLCSRM	1.17	0.55	1.72
SLMCSRM	1.12	1.20	2.32

The resulting losses from this method are summarised in TABLE IV. It is found that the FPSRM has the highest stator iron loss while the MCSRM has the lowest stator iron loss at this operating condition. This is mainly due to the fact that all the SRMs have the same stator flux density frequency while the FPSRM has the highest variation of both stator B_t and B_r, as shown in Fig. 11. Point C1 in the stator is not presented since the variation is only occurred in B_r. Despite the complicating factor of the different frequencies in the rotor, the same trend is observed for the rotor iron losses of FPSRM and MCSRM.

As is the case with all singly excited machines, the magnitude of the iron loss are increased markedly with the magnitude of the stator current. A comparison of iron losses as functions of phase RMS currents and rotor speeds are shown in Fig. 12. At rated speed and modest current (< 10A), the MCSRM has the lowest iron loss while the FPSRM has the highest iron loss. However, with increasing phase RMS current the iron losses increase more slowly in SLCSRM, CSRM and FPSRM, behaviour which can be attributed to the different means in which magnetic comes into play. At rated current, and with increasing rotor speed, the iron loss of MCSRM is the lowest with FPSRM the highest.

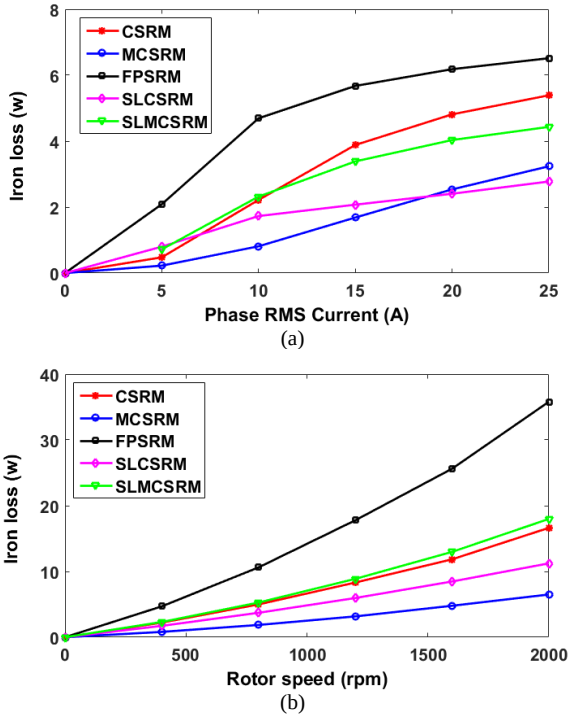

Fig. 12. Comparison of iron loss amongst SRMs. (a) at rated speed with increasing phase RMS current, (b) at rated current with increasing rotor speed.

However, as would be expected in these relatively small machines operating at modest speeds, the absolute levels of iron losses in all the machine topologies are very small in comparison with the copper losses shown previously in TABLE II. Nevertheless, the relative magnitudes of the iron losses for the various topologies provide a valuable and, within reason, a scalable indicator of their relative performance in applications where iron losses is likely to be a substantially more important discriminator, e.g. larger and higher speed machines.

IV. Comparison of Dynamic Performance

A. Torque Speed Characteristics

As already observed in Fig. 6, different winding structures lead to a range of different d- and q-axis inductances, which will in turn influence aspects of the machine dynamic performance, e.g. torque, power and power factor. In this analysis, the widely used circle diagram approach is adopted to establish the torque speed characteristic of each design variant [29]. Under flux

weakening control, the phase voltage and phase current limitation determines the maximum torque capability:

$$V_a = \sqrt{{V_d}^2 + {V_q}^2} \le V_{max} \quad (10)$$

$$I_a = \sqrt{{I_d}^2 + {I_q}^2} \le I_{max} \quad (11)$$

where V_a and I_a are the phase peak voltage and current.

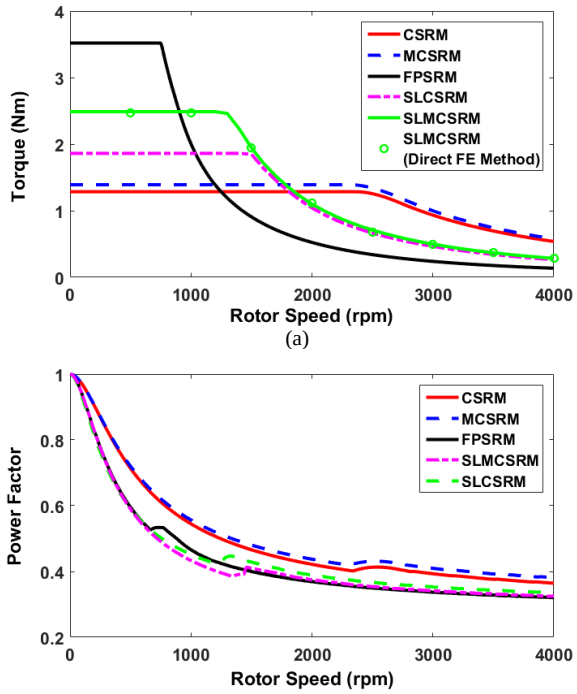

Fig. 13. Comparison of dynamic performance. $I_{max} = 14.14A$, and $V_{DC} = 100V$. (a) torque-speed curves, (b) power factor-speed curves.

Using the d- and q-axis inductances derived previously from equations (3)-(6) and (10)-(11), the torque speed curves Fig. 13 (a) were obtained. In each case, the maximum current, I_{max}, is 14.14A ($10A_{rms}$) and the DC link voltage, V_{DC}, is 100V ($V_{max} = \frac{2}{\pi}V_{dc}$). The method employed to account for the influence of cross-coupling is same to that has been proposed in [22].

It will be apparent from Fig. 13 that the FPSRM has highest initial torque, but the lowest base speed, i.e. the speed at which the torque begins to reduce. It can also be observed that the double layer CSRM and MCSRM have higher base speeds than their single layer counterparts. In order to validate the circle diagram approach used to derive these torque speed curves, the torque-speed curve for the SLMCSRM was calculated by the direct FE method (introduced in [22]). The Fig. 13 (a) shows a good agreement between the two methods.

A comparison of the variations in power factors with speed under the same current and voltage limitations ($10A_{rms}$ and 100V) is shown in Fig. 13 (b). Since the machines have different winding structures and hence different values of L_d and L_q, their power factors will also show some variation. With approximate end-winding structure and hence similar phase resistance, double layer CSRM and MCSRM have higher power factor than SLCSRM and SLMCSRM at the same rotor speed, in large part because of their lower L_d and L_q.

B. Efficiency Map

Efficiency maps for the various machines can be calculated from the torque speed characteristics and losses calculated previously using:

$$\eta = \frac{P_{out}}{P_{out} + P_{copper} + P_{iron} + P_{mech}} \times 100\% \quad (12)$$

where

P_{out} the output power is given by $\frac{\omega T}{p}$.

P_{mech} is the mechanical loss which consists of aerodynamic windage and bearing losses. It is independent of the load but depends on the rotor speed, air-gap and the axial lengths. According to [30], mechanical losses were calculated to be 2.64w at 400RPM for all the SRMs of identical size. The mechanical losses will increase with rotor speed since the bearing loss and windage losses are proportional to Ω (rotor velocity) and Ω^3, respectively.

Efficiency maps for the double layer, single layer and fully-pitched machines are compared in Fig. 14, respectively (regions with efficiency below 50% are not shown). For this specific series of designs, a maximum efficiency of 76% is achieved by double layer MCSRM between 6000 and 8000 rpm. Of the remaining topologies, the CSRM also achieves its maximum efficiency towards the upper end of the speed range. In contrast, the single-layer CSRM and MCSRM achieve their maximum efficiencies (some 75%) over the speed range of 3000 to 4500 rpm. Finally, the FPSRM has a more modest efficiency of 66%, which is achieved at lower rotor speed of around 2000 rpm. It is important to caution that these general trends in efficiency are to some degree specific to the small size of these reference designs, in particular that copper loss tends to dominate over iron loss in small machines.

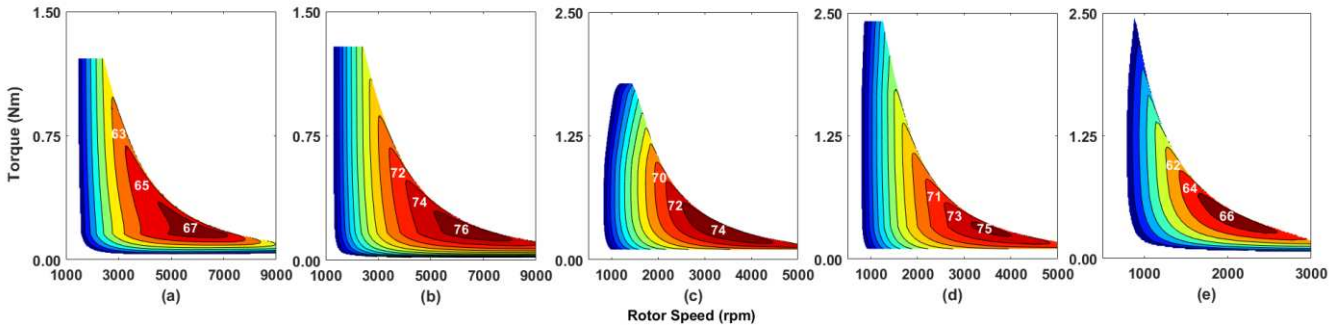

Fig. 14. Efficiency maps of SRMs when $I_{max} = 14.14A$, and $V_{DC} = 100V$. (a) CSRM, (b) MCSRM, (c) SLCSRM, (d) SLMCSRM, and (e) FPSRM.

V. Experimental Validation

A. Prototypes of SRMs

In order to validate the torque capability of double layer and single layer CSRM and MCSRM, two machines with the design specifications shown previously in TABLE I were constructed. Fig. 15 (a) shows the wound stator of a 12-slot/8-pole double layer CSRM and MCSRM while Fig. 15 (b) shows the stator for the SLCSRM and SLMCSRM. The conventional and mutually coupled SRMs can be realized with the same stator core and coils through a simple reconnection of the individual coils as detailed in Fig. 2 and Fig. 3. The common rotor of all the single and double layer variants is shown in Fig. 15 (c).

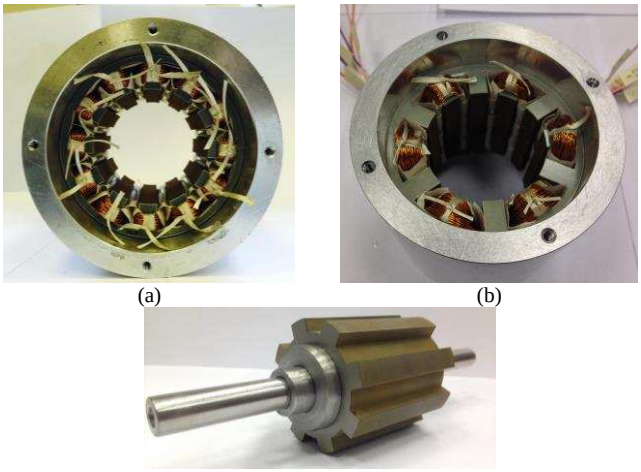

(a) (b) (c)

Fig. 15. 12-slot/8-pole prototype SRMs. (a) double layer CSRM or MCSRM stator, (b) SLCSRM or SLMCSRM stator, (c) 8-pole rotor.

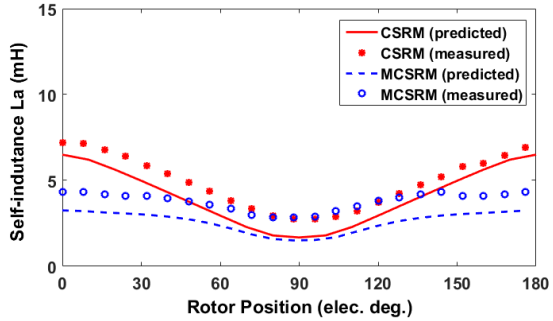

(a)

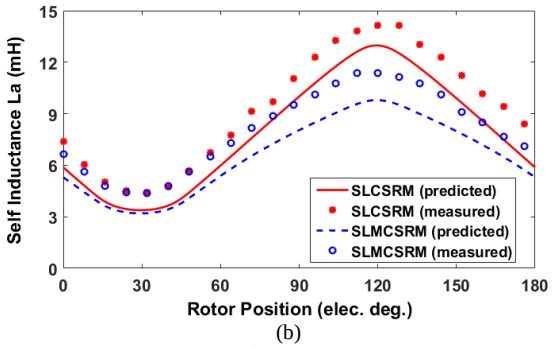

(b)

Fig. 16. Predicted and measured self-inductances versus rotor position at 1A DC phase peak current. (a) Double layer CSRM and MCSRM. (b) Single layer CSRM and MCSRM.

B. Measurement of Static Torque

The measured phase resistances are 1.48 Ω and 1.32 Ω for single and double layer SRMs respectively. Moreover, the self-inductances at 1A dc phase current are shown in Fig. 16. The method of static torque measurement detailed in [31] was adopted for undertaking all torque measurements in this study. During the tests, three phases of the SRMs are supplied by dc currents such as $I_A = I$, $I_B = -1/2I$ and $I_C = -1/2I$, where I is variable and controllable by the power supply. Fig. 17 shows the comparison of predicted and measured static torques at 10A DC current versus rotor angular positions (equivalent to current phase advanced angle when 3 phases are supplied by sinewave currents). Although the waveforms of static torque are not smooth and not sinusoidal due to torque ripple and measurement error, a good agreement can still be observed between the predicted and measured results.

Fig. 18 shows a comparison between predicted and measured static torques for phase peak currents between 1A and 10A. In this series of torque measurements, the rotor was fixed in an angular position which corresponds to the maximum average torque (45 elec. deg. if magnetic saturation does not occur).

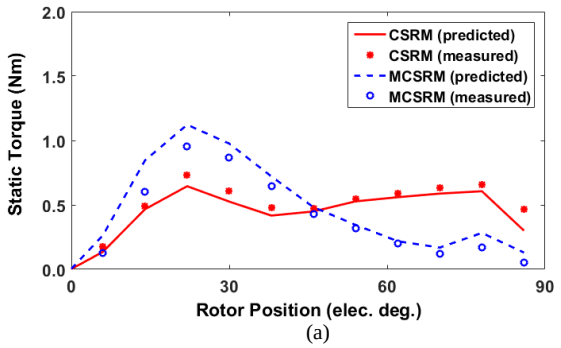

(a)

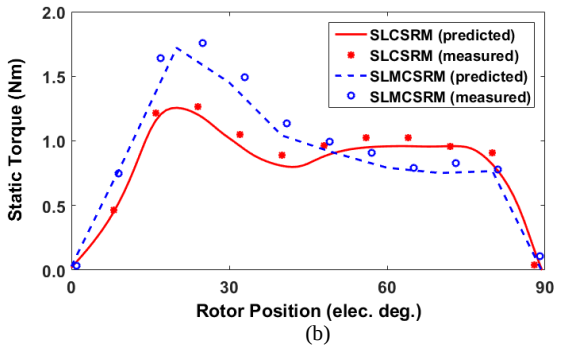

(b)

Fig. 17. Predicted and measured torques versus rotor position at 10A DC phase peak current. (a) Double layer CSRM and MCSRM. (b) Single layer CSRM and MCSRM.

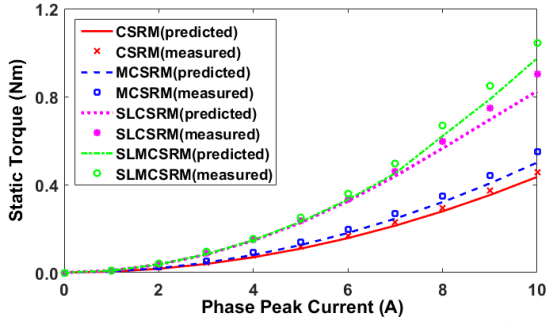

Fig. 18. Predicted and measured variation in static torque as a function of phase peak current.

C. Dynamic Tests

Dynamic tests have been carried out according to the method established in [32]. The dc link voltage for all dynamic tests is 18V and the maximum phase peak current is 6A, which is limited by the load torque capacity of the dc

machine. By way of example, tested current waveform of phase A and PWM line voltage (between phases A and B) for one electrical period of SLMCSRM are shown in Fig. 19.

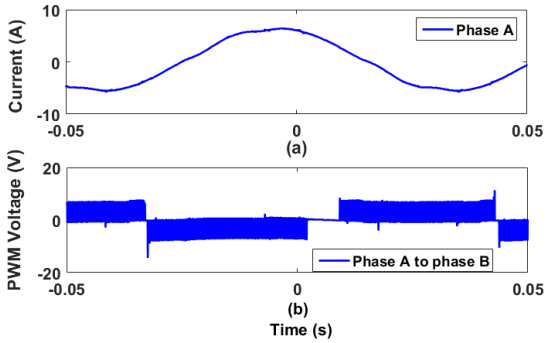

Fig. 19. Measured phase current and line voltage of SLMCSRM (a) phase A current, (b) PWM line voltage.

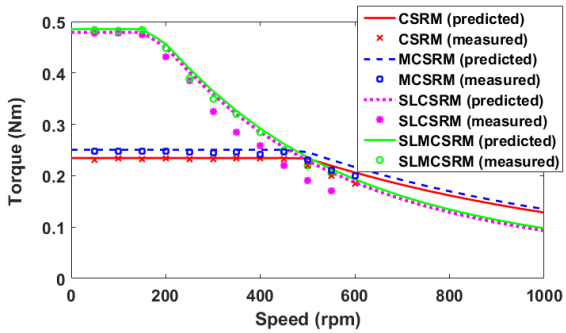

Fig. 20. Predicted and measured torque speed curves of double and single layer SRMs. $I_{max} = 6A$, and $V_{DC} = 18V$.

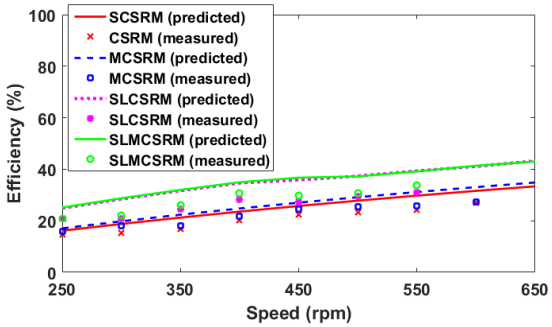

Fig. 21. Predicted and measured efficiency-speed curves. $I_{max} = 6A$, and $V_{DC} = 18V$.

Fig. 20 and Fig. 21 show the comparison of predicted and measured torque-speed and efficiency-speed curves for both single and double layer SRMs. The measured results match well with the simulated ones. The difference is mainly due to the fact that the end-winding effect has not been taken into account in 2D FEM. The torque sensor accuracy and measuring error are other influencing factors that contribute to this discrepancy. It is also worth mentioning that the low efficiency is mainly due to the fact that for the prototype machines, smaller copper wires have been used to ease the winding process, leading to smaller slot filling factor and higher copper loss.

VI. Conclusion

The static and dynamic performance of two double layer (CSRM and MCSRM) and two single layer (SLCSRM and SLMCSRM) short pitched SRMs, as well as one single layer fully pitched SRM (FPSRM), have been comprehensively investigated, principally through simulation and FE modelling, also experimental measurements of static torque and dynamic characteristics. It has been demonstrated, albeit within the context of relatively small machine dimensions, that at low phase current, the FPSRM produces lower copper loss per unit of average torque. However, due to the onset magnetic saturation, the performance of FPSRM deteriorates markedly with increasing phase RMS current. Additionally, due to its inherently higher iron loss across the full speed range, FPSRM achieves only modest performance at high speed.

Due to its reduced propensity for magnetic saturation, the double layer MCSRM performs well at high current levels, producing higher average torque than FPSRM for the same copper loss.

From a dynamic perspective, within the contest of this particular design study, the double layer MCSRM yields the lowest iron loss and the highest peak efficiency. The SLCSRM and SLMCRM produce higher average torque with lower torque ripple than their double layer counterparts at low phase current. However, in common to the FPSRM design, both the SLCSRM and SLMCSRM are prone to the onset of significant magnetic saturation with increasing phase current, making them less attractive at high phase current than a double layer MCSRM.

References

[1] T. J. E. Miller, "Optimal design of switched reluctance motors," IEEE Trans. Ind. Electron., vol. 49, no. 1, pp. 15-27, Feb. 2002.

[2] A. L. M. d. Santos, J. Anthonis, F. Naclerio, J. J. C. Gyselinck, H. V. d. Auweraer and L. C. S. Goes, "Multiphysics NVH modeling: simulation of a switched reluctance motor for an electric vehicle," IEEE Trans. Ind. Electron., vol. 61, no. 1, pp. 469-476, Jan. 2014.

[3] W. Hua, H. Hua, N. Dai, G. S. Zhao and M. Cheng, "Comparative study of switched reluctance machines with half-and full-teeth-wound windings," IEEE Trans. Ind. Electron., vol. 63, no. 3, pp. 1414-1424, Feb. 3, 2016.

[4] S. R. M. Aghdam, M. R. Feyzi, N. Bianchi and M. Morandin, "Design and analysis of a novel high-torque stator-segmented SRM," IEEE Trans. Ind. Electron., vol. 63, no. 3, pp. 1458-1466, Mar. 2016.

[5] X. B. Liang., G. J. Li, J. Ojeda, M. Gabsi and Z. X. Ren, "Comparative study of classical and mutually coupled switched reluctance motors using multiphysics finite-element modeling," IEEE Trans. Ind. Electron., vol. 61, no. 9, pp. 5066-5074, Sep. 2014.

[6] D. E. Cameron, J. H. Lang and S. D. Umans, "The origin and reduction of acoustic noise in doubly salient variable-reluctance motors," IEEE Trans. Ind. Appl., vol. 28, pp. 1250-1255, Nov./Dec. 1992.

[7] C. Wei, P. Pillay, Z. J. Tang and A. M. Omekanda , "Low-vibration design of switched reluctance motors for automotive applications using modal analysis," IEEE Trans. Ind. Appl., vol. 39, no. 4, pp. 971-977, Jul./ Aug. 2003.

[8] H. Y. Yang, Y. C. Lim and H. C. Kim, "Acoustic noise/ vibration reduction of a single-phase SRM using skewed stator and rotor," IEEE Trans. Ind. Electron., vol. 60, no. 10, pp. 4292-4300, Oct. 2013.

[9] J. W. Ahn, S. J. Park and D. H. Lee, "Hybrid excitation of SRM for reduction of vibration and acoustic noise," IEEE Trans. Ind. Electron., vol. 51, no. 2, pp. 374-380, Apr. 2004.

[10] C. Y. Wu and C. Pollock, "Analysis and reduction of vibration and acoustic noise in the switched reluctance drive," IEEE Trans. Ind. Appl., vol. 31, no. 1, pp. 91-98, Jan./Feb. 1995.

[11] D. H. Cameron, J. H. Lang and S. D. Umans, "The origin and reduction of acoustic noise in doubly salient variable-reluctance motors," IEEE Trans. Ind. Appl., vol. 26, no. 6, pp. 1250-1255, Dec. 1992.

[12] X. Ojeda, X. Mininger, H. B. Ahmed, M. Gabsi and M. Lecrivain, "Piezoelectric actuator design and placement for switched reluctance motors active dampling," IEEE Trans. Energy Convers., vol. 24, no. 2, pp. 305-313, Jun. 2009.

[13] X. Mininger, N. Galopin, X. Ojeda, F. Bouillault and M. Gabsi, "Modeling of magnetoelastic and piezoelectric coupling: Application to SRM noise damping," IEEE Trans. Magn., vol. 45, no. 3, pp. 1218-1221, Mar. 2009.
[14] J. Ahn, S. Oh, J. Moon and Y. Hwang, "A three-phase switched reluctance motor with two-phase excitation," IEEE Trans. Ind. Appl., vol. 35, no. 5, pp. 1067-1075, 1999.
[15] X. Ojeda, X. Mininger, M. Gabsi and M. Lecrivain, "Sinusoidal feeding for switched reluctance machine: application to vibration," in Proc. ICEM, Vilamoura, Portugal, Sep. 2008.
[16] X. Liu, Z. Q. Zhu, M. Hasegawa, A. Pride and R. Deodhar, "Investigation of PWMs on vibration and noise in SRM with sinusoidal bipolar excitation," in 21st IEEE-ISIE, Hangzhou, China, 28- 31 May, 2012.
[17] G. J. Li, J. Ojeda, S. Hlioui, E. Hoang, M. Lecrivain and M. Gabsi, "Modification in rotor pole geometry of mutually coupled switched reluctance machine for torque ripple mitigating," IEEE Trans. Magn., vol. 48, no. 6, pp. 2025-2034, Jun. 2012.
[18] X. Y. Ma, G. J. Li, G. Jewell and Z. Q. Zhu, "Comparative study of short-pitched and fully-pitched SRMs supplied by sine wave currents," in ICIT15, Sevilla, Spain, Mar. 2015.
[19] B. C. Mecrow, "Fully pitched-winding switched reluctance and stepping-motor arrangements," IET Elec. Power Appl., vol. 40, no. 1, pp. 61-70, Jan. 1993.
[20] B. C. Mecrow, "New winding configurations for doubly salient reluctance machines," IEEE Trans. Ind. Appl., vol. 32, no. 6, pp. 1348-1356, Dec. 1996.
[21] G. J. Li, J. Ojeda, E. Hoang, M. Lecrivain and M. Gabsi, "Comparative studies between classical and mutually coupled switched reluctance motors using thermal-electromagnetic analysis for driving cycles," IEEE Trans. Magn., vol. 47, no. 4, pp. 839-847, Apr. 2011.
[22] G. Qi, J. T. Chen, Z. Q. Zhu, D. Howe, L. B. Zhou and C. L. Gu, "Influence of skew and cross-coupling on flux-weakening performance of permanent-magnet brushless AC machines," IEEE Trans. Magn., vol. 45, no. 5, pp. 2110-2117, May 2009.
[23] R. R. Moghaddam, F. Magnussen and C. Sadarangani, "Theoretical and experimental reevaluation of synchronous reluctance machine," IEEE Trans. Ind. Electron., vol. 57, no. 1, pp. 6-13, Jan. 2010.
[24] D. A. Staton, T. J. E. Miller and S. E. Wood, "Maximising the saliency ratio of the synchronous reluctance motor," Elec. Power Appl, IEE Proc. B, vol. 140, no. 4, pp. 249-259, Jul. 1993.
[25] T. A. Lipo, "Synchronous reluctance machines- a viable alternative for AC drives," Wisconsin electric machines and power electronics consortium, Madison, USA, May 1991.
[26] S. D. Calverley, G. W. Jewell and R. J. Saunders, "Prediction and measurement of core losses in a high-speed switched-reluctance machine," IEEE Trans. Magn., vol. 41, no. 11, pp. 4288-4298, Nov. 2005.
[27] Y. Hayashi and T. J. E. Miller, "A new approach to calculating core losses in the SRM," IEEE Trans. Indus. Appl., vol. 31, no. 5, pp. 1039-1046, 1995.
[28] Q. Yu, B. Bilgin and A. Emadi, "Loss and efficiency analysis of switched reluctance machines using a new calculation method," IEEE Tran. Ind. Electron, vol. 62, no. 5, pp. 3072-3080, May, 2015.
[29] W. L. Soong and T. J. E. Miller, "Field-weakening performance of brushless synchronous AC motor drives," IEE Proc.-Electr. Power Appl., vol. 141, no. 6, pp. 331-340, Nov. 1994.
[30] J. Pyrhonen, T. Jokinen and V. Hrabovcova, "Design of rotating electrical machines", Chichester, UK: John Wiley & Sons, 2008.
[31] Z. Q. Zhu, "A simple method for measuring cogging torque in permanent magnet machines," in IEEE Power & Energy Society General Meeting,, Jul. 26-30, 2009, pp. 1-4.
[32] T. S. Kwon and S. K. Sul, "Novel antiwindup of a current regular of a surface-mounted permanent-magnet motor for flux-weakening control," IEEE Trans. Ind. Appl., vol. 42, no. 5, pp. 1293-1300, Sep./Oct. 2006.

X. Y. Ma received the B.Eng. degree in electrical engineering from The University of Sheffield, Sheffield, U.K., in 2012, and the M.Sc. degree in sustainable energy systems from The University of Edinburgh, Edinburgh, U.K., in 2013. She is currently working toward Ph.D. degree in the Department of Electronic and Electrical Engineering, The University of Sheffield, Sheffield, U.K. Her current research interest is switched reluctance machines.

G. J. Li (M'10) received his BEng, MSc and PhD degrees in electrical and electronic engineering from the Wuhan University, China, in 2007, University of Paris XI, France, in 2008, and the Ecole Normale Supérieure (ENS) de Cachan, Paris, France, in 2011, respectively. He joined the University of Sheffield in June 2012 as a post-doctoral research associate at EMD Group. Since September 2013, he took up a Lectureship in Electrical Engineering within the EMD Group at the University of Sheffield. His main research interests include the design, fault analysis and thermal management of electrical machines for renewable energy, automotive, more electrical aircraft, etc.

G. W. Jewell received the B.Eng. and Ph.D. degrees in Electrical Engineering from The University of Sheffield, Sheffield, U.K., in 1988 and 1992, respectively. Since 1994, he has been a member of Academic Staff in the Department of Electronic and Electrical Engineering, The University of Sheffield, where he is currently a Professor of Electrical Engineering, Head of Department and Director of the Rolls-Royce University Technology Centre in Advanced Electrical Machines. His research interests include the modelling and design of a wide variety of electromagnetic devices, notably electrical machines for aerospace and high-temperature applications. Professor Jewell held an Engineering and Physical Sciences Research Council Advanced Research Fellowship from 2000 to 2005 and a Royal Society Industry Fellowship with Rolls-Royce from 2006 to 2008.

Z. Q. Zhu (M'90-SM'00-F'09) received the B.Eng. and M.Sc. degrees from Zhejiang University, Hangzhou, China, in 1982 and 1984, respectively, and the Ph.D. degree from the University of Sheffield, Sheffield, U.K., in 1991, all in electrical engineering.

Since 1988, he has been with the University of Sheffield, where he is currently Professor of electrical machines and control systems, Head of the Electrical Machines and Drives Research Group, Royal Academy of Engineering/Siemens Research Chair, Academic Direct of Sheffield Siemens Wind Power Research Centre, Director of CSR electric Drives Technology Research Centre. His current major research interests include design and control of permanent-magnet brushless machines and drives for applications ranging from automotive, domestic appliance, to renewable energy.

H. L. Zhan received the B.Eng. and the M.Sc. degrees in Electrical Engineering from Harbin Institute of Technology, Harbin, China, in 2012 and 2014, respectively. He is currently working toward Ph.D. degree with the Department of Electronics and Electrical Engineering, the University of Sheffield, Sheffield, U.K.

His current research interests include permanent magnet synchronous motor drives and parameter identification